Microfluid Nanofluid
DOI 10.1007/s10404-009-0447-0

RESEARCH PAPER

A novel experimental setup for gas microflows

Jeerasak Pitakarnnop · Stelios Varoutis · Dimitris Valougeorgis · Sandrine Geoffroy · Lucien Baldas · Stéphane Colin

Received: 6 February 2009 / Accepted: 6 April 2009

Abstract A new experimental setup for flow rate measurement of gases through microsystems is presented. Its principle is based on two complementary techniques, called droplet tracking method and constant-volume method. Experimental data on helium and argon isothermal flows through rectangular microchannels are presented and compared with computational results based on a continuum model with second-order boundary conditions and on the linearized kinetic BGK equation. A very good agreement is found between theory and experiment for both gases, assuming purely diffuse accommodation at the walls. Also, some experimental data for a binary mixture of monatomic gases are presented and compared with kinetic theory based on the McCormack model.

J. Pitakarnnop · S. Geoffroy · L. Baldas · S. Colin (✉)
LGMT (Laboratoire de Génie Mécanique de Toulouse), INSA, UPS, Université de Toulouse, 135, avenue de Rangueil, 31077 Toulouse, France
e-mail: stephane.colin@insa-toulouse.fr

J. Pitakarnnop
e-mail: jeerasak.pitakarnnop@insa-toulouse.fr

S. Geoffroy
e-mail: sandrine.geoffroy@insa-toulouse.fr

L. Baldas
e-mail: lucien.baldas@insa-toulouse.fr

S. Varoutis · D. Valougeorgis
Department of Mechanical and Industrial Engineering, University of Thessaly, 38334 Volos, Greece

S. Varoutis
e-mail: svarouti@uth.gr

D. Valougeorgis
e-mail: diva@mie.uth.gr

Published online: 28 April 2009

Keywords Microfluidics · Rarefied gas flow · Experimental setup · Micro flow rate measurement · Discrete velocity method · Slip flow · Transition flow

1 Introduction

Rarefied gas flows have been intensively studied during the past decades due to a wide variety of applications. Specific experimental setups have been designed for measuring flow rates of low-pressure gas flows, in order to detect leaks (McCulloh et al. 1987; Bergoglio et al. 1995) or to analyse pumping speed (Jousten et al. 2002). For example, the Physikalisch–Technische Bundesanstalt (PTB) has designed a complex gas flowmeter able to measure gas flow rates between 4×10^{-13} and 10^{-6} mol s^{-1} for very low-pressure conditions, between 10^{-10} and 3×10^{-2} Pa. Recently, improvements in micro fabrication techniques have contributed to the rapid development of microfluidics, and the experimental analysis of rarefied gases in microsystems is now of great interest even at atmospheric pressure, or in moderate vacuum conditions. The lack of experimental data about gas flows in microchannels has motivated researchers for developing specific setups dedicated to rarefied gas microflows.

Two main kinds of solutions are proposed in the literature:

- Several authors have developed a method based on the tracking of a liquid droplet (Pong et al. 1994; Harley et al. 1995; Lalonde 2001; Zohar et al. 2002; Maurer et al. 2003; Colin et al. 2004; Ewart et al. 2006). In this method, the droplet is pushed by the gas flow, and its tracking allows a direct measurement of the volume flow rate.

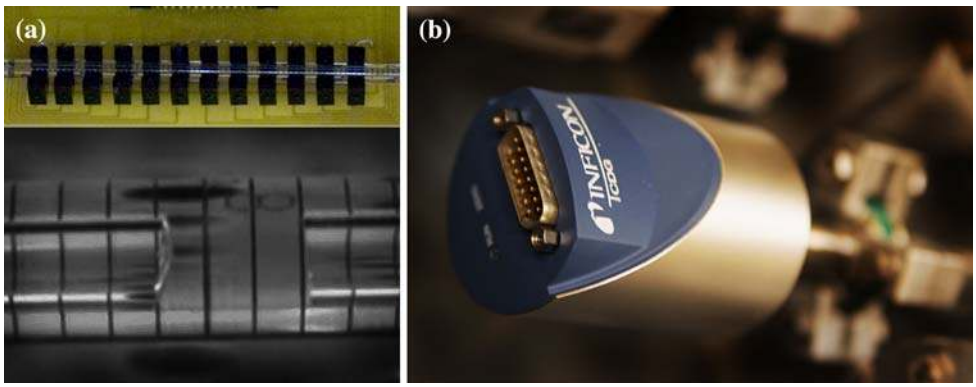

Fig. 1 **a** Series of opto-electrical sensors and glycerol droplet inside the calibrated pipette (for DT method). **b** Inficon® capacitance diaphragm gauge (for CV method)

- Other authors have developed indirect measurement techniques using the gas equation of state, generally assumed as an ideal gas. In a temperature-regulated surrounding, mass flow rates can be deduced from the measurement of volume or pressure variations (with the so-called constant-pressure and constant-volume techniques). The constant-pressure technique is technologically difficult to implement, and it requires, for example, the use of a piston or a bellow controlled by an automation system to allow volume variation while maintaining a constant pressure (McCulloh et al. 1987; Jousten et al. 2002). On the other hand, setups built for constant-volume technique are less complicated, as only the pressure variation measurement inside a tank is required (Ewart et al. 2006). However, such systems could be very sensitive to thermal fluctuations.

The experimental setup presented in this article integrates these two techniques (droplet tracking and constant-volume methods, respectively, called DT and CV methods) in the same experimental ring for double-checking the flow rate measurement at both the inlet and the outlet of the microsystem. The goal is an improvement of the data accuracy. Two series of 12 opto-electrical sensors and high-sensitivity pressure transducers are used for tracking droplets movements and detecting small pressure variations, respectively. The setup can operate in a range from a few mbars to a few bars. Experimental data relative to flows of helium (He), argon (Ar), and He–Ar mixtures through silicon rectangular microchannels are presented and analysed. A comparison study between experimental results and corresponding computational ones is provided.

2 Experimental setup

2.1 Description of the experimental setup

The experimental setup is able to measure gas flow rates using two different methods. In the first method (DT method), volume flow rates are deduced from tracking a liquid droplet inside a calibrated pipette. As shown in Fig. 1a, a series of 12 opto-electrical sensors are used to detect the movement of the droplet. In the second method (CV method), pressure and temperature variations are measured during the flow, and the mass flow rate is deduced from the gas equation of state. In this study, we focus on isothermal flows, and the setup is thermally regulated. Figure 1b shows one of the Inficon® capacitance diaphragm gauges used for accurately measuring the pressure variation. The range of the gauge is chosen according to the inlet and outlet pressure levels. The specifications of the gauges used in this study are given in Table 1.

The CV method does not use any mechanical moving part, which makes this method simpler and limits the numbers of measurement components. The DT method could sometimes be trickier to implement, as the droplet could experience some unpredictable behaviours, due to small wall flaws. However, the CV method is more sensitive to small thermal fluctuations; this is why Arkilic et al. developed a specific technique with two tanks drilled inside the same piece of copper (Arkilic et al. 2001). Our setup is thermally regulated by means of two Peltier modules, which allow maintaining a constant and uniform temperature inside the whole setup.

Figure 2 shows a diagram of this experimental setup. The microsystem (e.g. a microchannel or a series of microchannels) is connected via the valve V3A to the upstream circuit A and via the valve V3B to the downstream circuit B. If necessary, the role of circuits A and B may be inverted, B becoming the upstream circuit. Each

Table 1 Specifications of Inficon® capacitance diaphragm gauges

Full scale (Pa)	1.333E + 3	1.333E + 4	1.333E + 5
Maximum pressure (Pa)	1.333E + 3	1.333E + 4	1.333E + 5
Minimum pressure (Pa)	1.333E + 2	1.333E + 3	1.333E + 4
Accuracy	0.2% of reading		
Resolution	0.0015% of full scale		

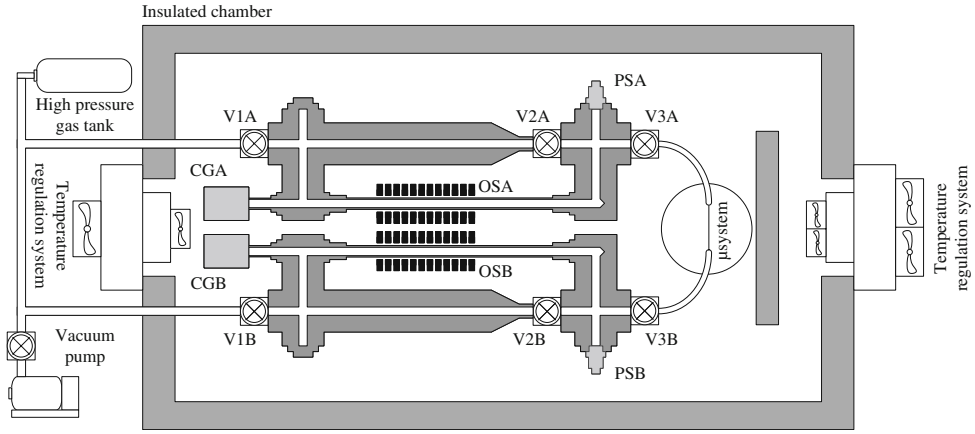

Fig. 2 Diagram of the test setup (electrical wiring, temperature sensors and data acquisition system are not shown)

circuit A or B includes three valves, V1, V2 and V3, one calibrated pipette—into which a liquid drop has been previously put—equipped with opto-electrical sensors OS, one Kulite® piezoresistive pressure sensor PS, and one Inficon® high-sensitivity capacitance diaphragm gauge CG. Every valve being open, the whole circuit can be outgassed using a vacuum pump. Then, valves VA3 and/or VB3 are closed and the upstream and downstream circuits are filled with gas from a high-pressure tank. This step is repeated several times, in order to be sure that eventual traces of previous gases, including gas adsorbed at the walls of the circuits, are removed and that the only gas remaining inside the setup is the operating gas for flow rates measurements. The pressure level is independently controlled in each circuit with a pressure regulator, and then valve V1 is closed. After waiting some time until thermal equilibrium is reached, valve V2 is closed and valve V3 is opened allowing the gas flow from circuit A to circuit B, through pipette A, the microsystem and pipette B.

Two series of 12 opto-electrical sensors OSA and OSB are used to track the two droplets pushed upstream and downstream by the gas flow. The inner surfaces of the calibrated pipettes have been submitted to a hydrophobic treatment to avoid droplet breakup or formation of a liquid film at the wall during the droplet movement. A series of individual measures of the volume flow rate can be obtained, which allows determining the mean volume flow rates upstream and downstream from the microsystem, and consequently, the mass flow rate through the microsystem. The comparison of the individual data given by each couple of opto-electrical sensors, as well as the comparison of the two mean mass flow rates deduced from the two mean volume flow rates, must be consistent with the experimental uncertainties, for validating the data (DT method). The main uncertainty for the DT method concerns the distances (0.1%) between each opto-electrical sensors, the volume of the pipettes (1%) and the distances between each graduation of the pipette (2%), leading to a $\pm 3.1\%$ overall uncertainty.

During the measurements, upstream and downstream pressures are submitted to a small (typically 1–2%) decrease and increase, respectively. The pressure variations allow determining the mass flow rate with the CV method.

The volumes of circuits A and B have been accurately measured with a specific setup, shown in Fig. 3. The volume A (or B) is initially pressurized and it is connected to a

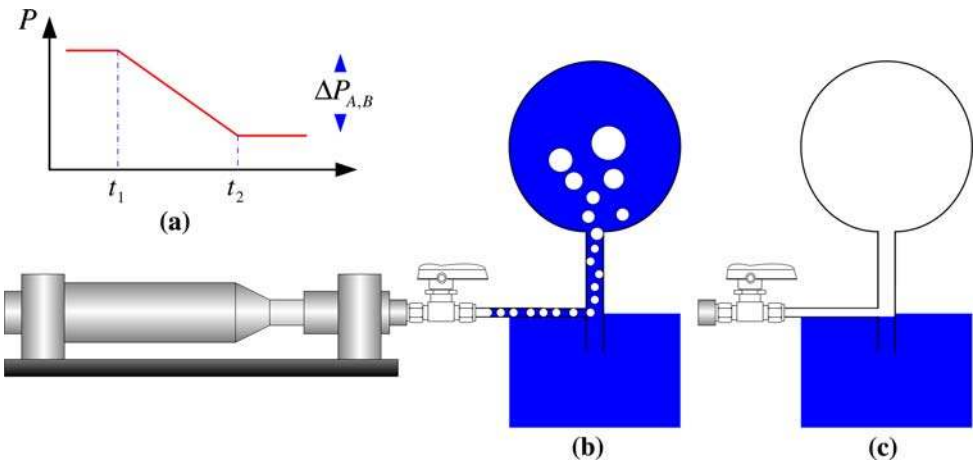

Fig. 3 Diagram of the specific setup for measurement of volumes V_A and V_B. **a** Pressure variation in circuit A or B; **b** beginning of the process ($t = t_1 + \varepsilon$); **c** end of the process ($t = t_2$)

balloon using a tube with a small diameter. This balloon has been previously filled with water and turned upside down on a basin of water. The connection of the small tube is at the level of the water surface, such that the pressure inside the tube is equal to the atmospheric pressure P_{atm}. The valve is opened at $t = t_1$ to allow the air flow from the circuit A (or B) towards the balloon (Fig. 3b). The balloon is slowly filled with air and the valve is closed at $t = t_2$ when all the water inside the balloon has been replaced with air (Fig. 3c). During this process, the pressure $P_{A,B}$ inside the volume A (or B) is monitored with a piezoresistive sensor PS (see typical pressure signal in Fig. 3a). The volume $V_{A,B}$ of the circuit A (or B) can then be deduced from the mass conservation, assuming that air behaves as an ideal gas, by the equation

$$V_{A,B} = \frac{P_{atm} V_{balloon}}{\Delta P_{A,B}} \tag{1}$$

where $\Delta P_{A,B}$ is the pressure variation inside the volume A (or B) between times t_1 and t_2. The volume $V_{balloon}$ includes the volume of the balloon and the volume of the tube between the valve and the balloon. This volume has been measured by weighting the balloon and the tube before and after filling them with water. The uncertainty on the volume of circuit A (or B) is then estimated as:

$$\frac{\Delta V_{A,B}}{V_{A,B}} = \frac{\Delta(\Delta P_{A,B})}{\Delta P_{A,B}} + \frac{\Delta P_{atm}}{P_{atm}} + \frac{\Delta V_{balloon}}{V_{balloon}} = \pm(0.5 + 0.5 + 0.3)\% = \pm 1.3\%. \tag{2}$$

According to the range of the measured flow rate and the duration of the measure, these volumes can be adjusted changing some internal parts of circuits A and B between valves V1 and V2.

The temperature variation is measured during the operations with four PT100 temperature sensors (with a 0.15 K accuracy), and the deviation during each experiment is less than 0.1 K. The temperature inside the insulated chamber is homogeneous with deviations less than 0.6 K.

Most of the setup is made of stainless steel, aluminium or glass, and the connections are insured by ISO-KF and Swagelok's Ultra-Torr® components to avoid any leakage during low-pressure operation. Air tightness has been checked by means of He detection, with a portable high precision leak detector.

2.2 Flow rate calculation

2.2.1 CV method

With the constant volume method, the mass flow rate is calculated from the ideal-gas equation of state

$$\frac{dM}{dt} = \frac{d}{dt}\left(\frac{PV}{RT}\right) \tag{3}$$

applied to circuit A or B, where M, V, P, R, T and t are, respectively, the mass of the gas in the circuit, the constant volume of the circuit, the pressure, the specific gas constant, the temperature and the time. The mass flow rate through the microsystem is then given by (Arkilic et al. 2001; Ewart et al. 2006)

$$\dot{M} = \frac{V}{RT}\frac{dP}{dt}\left(1 - \frac{dT/T}{dP/P}\right). \tag{4}$$

As mentioned earlier, this method requires a high-thermal stability, ensured by two temperature-regulation systems (see Fig. 2). The standard deviation of the temperature is in all cases around 0.1 K. The relative temperature variation dT/T is then of the order of 4×10^{-4} (see Fig. 4), to be compared with the relative pressure variation $dP/P \approx 2 \times 10^{-2}$. As a consequence, Eq. 4 is simplified as

$$\dot{M} = \frac{V}{RT} ac \tag{5}$$

where $a = dP/dt$ is calculated from a least-square linear fit of the measured pressure

$$P(t) = at + b \tag{6}$$

and $c = 1 - (dT/T)/(dP/P) = 1 \pm 2\%$. More than 1,000 pressure data are used for determining coefficients a and b. The standard deviation of coefficient a is calculated following the method proposed in (Ewart et al. 2006) and is found to be less than 0.5%. Therefore, the overall uncertainty of the mass flow rate measurement is calculated from

$$\frac{\Delta\dot{M}}{\dot{M}} = \frac{\Delta V}{V} + \frac{\Delta T}{T} + \frac{\Delta a}{a} + \frac{\Delta c}{c}, \tag{7}$$

and is less than $\pm(1.3 + 0.2 + 0.5 + 2)\% = \pm 4\%$.

2.2.2 Operating procedure and data processing for CV method

Outgassing from the setup when operating at low pressure could generally not be neglected, and consequently must be measured. Outgassing is first quantified in the downstream circuit B, including all connections up to the microsystem outlet. In order to avoid flow through the microsystem during this operation, both upstream and downstream circuits are pressurized to the downstream operating pressure before closing valve V3A. After registering with gauge CGB, the pressure rise in circuit B during a while (see 1st step in Fig. 5), pressure in circuit A is increased to the desired upstream value and the flow rate through the microsystem can be measured opening valve V3A. Following the flow rate

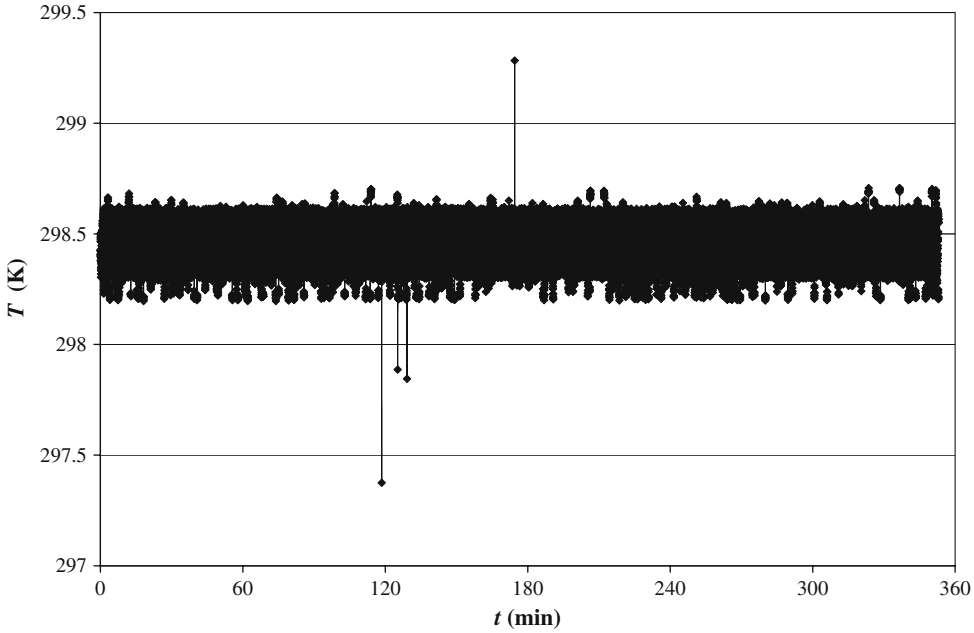

Fig. 4 Typical temperature evolution inside the insulated chamber

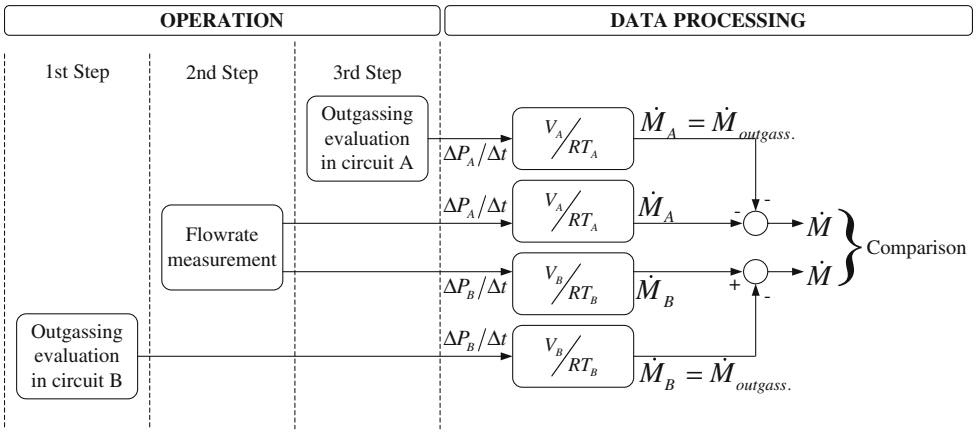

Fig. 5 Schematic representation of operating procedure and data processing (case for which A is the upstream circuit)

measurement (see 2nd step in Fig. 5), outgassing is quantified in circuit A, including all connections up to the microsystem inlet. For that purpose, pressure in circuit B is increased to the same level as in circuit A, to avoid flow through the microsystem due to a pressure gradient; then valve V3B is closed and the pressure rise in circuit A is monitored for some time by gauge CGA (see 3rd step in Fig. 5). The operating time of flow measurement ranges between several minutes and 2 h, depending on pressure conditions. However, the outgassing evaluation process could take around 3 h in order to detect a small pressure variation. During all this process, the test rig is kept at constant temperature as illustrated by Fig. 4 thus showing that the temperature inside the thermal box is not sensitive to possible variations of the room temperature. Figure 5 represents schematically the operating procedure and data processing for the CV method. Outgassing rates are calculated with Eq. 5 and used to correct the flow rate data. Outgassing is negligible for moderate Knudsen numbers (mean values less than 10^{-1}), but the corresponding flow rates can reach 60% of the real flow rates through the microchannels for the highest Knudsen numbers. The uncertainties shown in Eq. 7 are also taken into account for the calculation of the outgassed flow rate, and the total uncertainty represented by vertical bars in the following figures takes into account all uncertainties introduced in the three steps of the operating procedure shown in Fig. 5. As a consequence, for the highest values of the outlet pressure (50 kPa), the total uncertainty is ±4% as outgassing is negligible, and for lower outlet pressures for which outgassing is no longer negligible, the total uncertainty is given by

$$\frac{\Delta \dot{M}}{\dot{M}} = \pm 0.04\left(1 + 2\frac{\dot{M}_{\text{outgass.}}}{\dot{M}}\right) \tag{8}$$

where $\dot{M}_{\text{outgass.}}$ is the mass flow rate inside circuit A or B only due to outgassing (see Fig. 5). The uncertainties

calculated from Eq. 8 are given in Sects. 4.2 and 4.3. It should be outlined that outgassing is essentially due to the manufactured parts of circuits A and B, although outgassing from the walls of the microchannel can be neglected, first because silicon and glass wafers have very clean surfaces and second because the surface area of the microchannels' walls is typically ten orders of magnitude lower than the total surface area of circuits A or B.

Finally, the comparison of the upstream and downstream resulting flow rates is an indirect mean for checking that the outgassing effects are well taken into account by the procedure described in Fig. 5, whatever the level of outgassing.

2.3 Rectangular microchannels

The microsystems used for these first experiments consist of series of parallel rectangular microchannels etched by deep reactive ion etching (DRIE) in silicon wafers, and covered with Pyrex plates by anodic bonding.

Table 2 shows the characteristics of microsystem M2 used for this study. It is made of 45 parallel microchannels connected to upstream and downstream comb-shaped reservoirs with high depth ($\approx$300 μm). This layout shown in Fig. 6 increases the flow rate measurement accuracy while reducing the operation time. The range of the total mass flow rate is from 3×10^{-12} to 9×10^{-10} kg s^{-1}. The cross section of each rectangular microchannel is defined by $-W/2 \leq x \leq W/2$ and $-H/2 \leq y \leq H/2$. Its aspect ratio

Table 2 Specifications of microsystem M2

Microsystem	Depth, H (μm)	Width, W (μm)	Length, L (μm)	Number of microchannels
M2	1.88	21.2	5,000	45
Uncertainty	0.10	0.3	10	

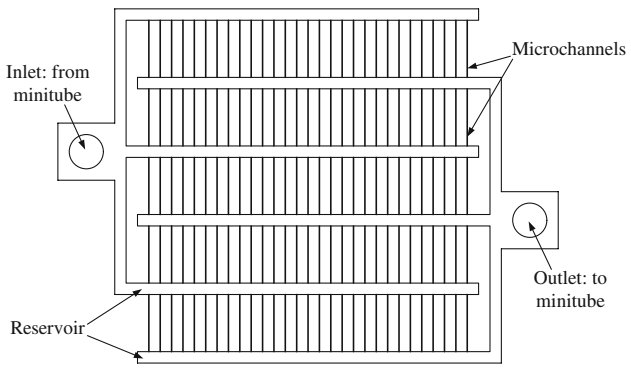

Fig. 6 Diagram of microchannels with their reservoirs

$a* = \frac{H}{W}$ is equal to 0.089. The depth shown in Table 2 and the roughness are measured by a TENCOR P1 profilometer. The typical roughness is between 50 and 80 Å. The initial uncertainty of the depth (0.1 μm) is finally reduced to 0.01 μm, after comparison between measured and simulated flow rates in the hydrodynamic regime, at low Knudsen numbers (Lalonde 2001).

3 Numerical simulations

Experimental data reported in this paper concern two different flow regimes. The first one is the slip flow regime with a Knudsen number between 10^{-3} and 10^{-1} and the second one is the transition regime with Knudsen numbers between 10^{-1} and 10. In this section, the corresponding numerical modeling for the two flow regimes implemented in the present work is described.

3.1 Continuum models—for slip flow regime

When the Knudsen number Kn, defined as the ratio of the mean free path, λ, of the molecules over the hydraulic diameter, D_h, of the microchannel, is in the range 10^{-3}–10^{-1}, local disequilibrium at the walls becomes significant and slip should be taken into account. Compressible Navier–Stokes equations are still valid, provided they are associated with velocity-slip and temperature-jump boundary conditions. For isothermal flow and limited values of the Knudsen number, classic first-order boundary conditions

$$u|_{x=\pm\frac{W}{2}} = \mp\beta\frac{2-\alpha}{\alpha}\lambda\left.\frac{\partial u}{\partial x}\right|_{x=\pm\frac{W}{2}} = \mp A_1\lambda\left.\frac{\partial u}{\partial x}\right|_{x=\pm\frac{W}{2}}$$
$$u|_{y=\pm\frac{H}{2}} = \mp\beta\frac{2-\alpha}{\alpha}\lambda\left.\frac{\partial u}{\partial y}\right|_{y=\pm\frac{H}{2}} = \mp A_1\lambda\left.\frac{\partial u}{\partial y}\right|_{y=\pm\frac{H}{2}} \quad (9)$$

are generally suitable for an accurate calculation of the mass flow rate, assuming a locally fully developed flow (Colin 2005). In Eq. 9, u is the streamwise velocity and $0 \leq \alpha \leq 1$ the tangential momentum accommodation coefficient, with $\alpha = 1$ and 0 denoting the purely diffuse and specular reflections, respectively. Also, β is a corrective coefficient calculated by different authors (Cercignani et al. 1994) who have shown that a better prediction of the flow out of the Knudsen layer would be obtained with this corrective coefficient, slightly different from unity, unlike as initially proposed by Maxwell (1879). For higher values of Kn, the accuracy can be improved using second-order boundary conditions. These conditions can involve normal and tangential second derivatives (Deissler 1964) and in the case of a rectangular microchannel take the form

$$u|_{x=\pm\frac{W}{2}} = \mp A_1 \lambda \left.\frac{\partial u}{\partial x}\right|_{x=\pm\frac{W}{2}} + A_2 \lambda^2 \left.\left(\frac{\partial^2 u}{\partial x^2} + B_2 \frac{\partial^2 u}{\partial y^2}\right)\right|_{x=\pm\frac{W}{2}}$$
$$u|_{y=\pm\frac{H}{2}} = \mp A_1 \lambda \left.\frac{\partial u}{\partial y}\right|_{y=\pm\frac{H}{2}} + A_2 \lambda^2 \left.\left(\frac{\partial^2 u}{\partial y^2} + B_2 \frac{\partial^2 u}{\partial x^2}\right)\right|_{y=\pm\frac{H}{2}}. \quad (10)$$

In the present paper, experimental data are compared with semi-analytical models of flows in rectangular microchannels based on boundary conditions (9) or (10). It is noted that the first-order coefficient in Eq. 10 is $A_1 = \beta(2 - \alpha)/\alpha$. Values of coefficients β, A_2 and B_2 are shown in Table 3. For first-order boundary conditions, the coefficient A_2 is zero. Maxwell (1879) proposed $\beta = 1$ and Cercignani and Daneri (1963) further obtained an improved value $\beta = 1.1466$ from the BGK equation. Deissler developed a second-order boundary condition valid for 3-D flows, with the coefficients $\beta = 1$, $A_2 = -9/8$ and $B_2 = 1/2$. Recently, Hadjiconstantinou (2003) suggested to keep the value $\beta = 1.1466$ from Cercignani and to modify A_2 as $A_2 = -0.647$. In this paper, we propose a modified second-order boundary conditions (see Table 3), taking into account the coefficients from Hadjiconstantinou, associated with the value $B_2 = 1/2$ proposed by Deissler. In all cases, the mean free path is calculated based on the hard sphere collision model (Chapman and Cowling 1952; Kandlikar et al. 2006).

Aubert and Colin (2001) proposed a semi-analytical model for calculating the mass flow rate through a rectangular microchannel using Deissler boundary conditions. After integration along the microchannel, the mass flow rate initially calculated as a function of the local pressure gradient can be obtained as a function of the total inlet over outlet pressure ratio $\Pi = \frac{P_A}{P_B}$:

$$\dot{M} = -\frac{4h^4}{a^* \mu L} \frac{P_B^2}{RT} \times \left(\frac{a_1(\Pi^2 - 1)}{2} + a_2 Kn_B(\Pi - 1) + a_3 Kn_B^2 \ln \Pi\right). \quad (11)$$

In Eq. 11, μ is the dynamic viscosity of the gas, subscript B refers to the outlet of the microchannel, the length of which is L, the coefficients (a_1, a_2, a_3) depend on the aspect ratio a^* and (a_2, a_3) depend on the accommodation coefficient α. For $a^* = 0.089$ and $\alpha = 0.9$,

$$a_{1(D)} = 0.3147;\ a_{2(D,\alpha=0.9)} = 2.3954;\ a_{3(D,\alpha=0.9)} = 4.1352 \quad (12)$$

are obtained from the model developed in (Aubert and Colin 2001). For $a^* = 0.089$ and $\alpha = 1$, their values are:

$$a_{1(D)} = 0.3147;\ a_{2(D,\alpha=1)} = 1.9819;\ a_{3(D,\alpha=1)} = 4.1344. \quad (13)$$

In Eqs. 12 and 13, subscript D refers to Deissler boundary conditions. The same semi-analytical model has been applied for the modified boundary conditions proposed earlier. For these boundary conditions, we obtain for $a^* = 0.089$ and $\alpha = 1$

$$a_{1(m)} = 0.3134;\ a_{2(m,\alpha=1)} = 2.2139;\ a_{3(m,\alpha=1)} = 2.4212. \quad (14)$$

In the present paper, experimental flow rates are compared with the values given by Eq. 11 and the coefficients associated to Deissler boundary conditions [Eqs. 12 or 13] or to the modified boundary conditions [Eq. 14].

3.2 Kinetic models—for whole Knudsen range

Solutions based on kinetic theory of gases are valid in the whole range of the Knudsen number from the free molecular, through the transition up to the slip and hydrodynamic regimes. The basic unknown is the distribution function, which obeys the Boltzmann equation or reliable and properly chosen kinetic model equations. Over the years, it has been shown that fully developed isothermal pressure driven flows, as the ones investigated in the present work, can be simulated efficiently by the linearized BGK equation, which in dimensionless form is written as (Sharipov 1999)

Table 3 Values of coefficients β, A_2 and B_2 for boundary conditions (9) or (10)

Author, year	β	A_2	B_2	Remarks
Maxwell, 1879 (Maxwell 1879)	1	0	–	First-order model
Cercignani, 1963 (Cercignani and Daneri 1963)	1.1466	0	–	From kinetic theory—BGK equation
Deissler, 1964 (Deissler 1964)	1	−9/8	1/2	Second-order model
Hadjiconstantinou, 2003 (Hadjiconstantinou 2003)	1.1466	−0.647	–	From kinetic theory—BGK equation
Modified second-order boundary conditions (present paper)	1.1466	−0.647	1/2	Deissler boundary conditions modified with Hadjiconstantinou's coefficients

$$c_x \frac{\partial \Phi}{\partial x} + c_y \frac{\partial \Phi}{\partial y} + \delta \Phi = \delta u - \frac{1}{2}. \tag{15}$$

Here, $\Phi = \Phi\ (x,\ y,\ c_x,\ c_y)$ is the reduced unknown distribution, while $(c_x,\ c_y)$ denote the components of the molecular velocity vectors in the x- and y-directions. Also,

$$u(x,y) = \frac{1}{\pi} \int_{-\infty}^{\infty} \int_{-\infty}^{\infty} \Phi \exp\left[-c_x^2 - c_y^2\right] \mathrm{d}c_x \mathrm{d}c_y \tag{16}$$

is the streamwise macroscopic (bulk) velocity. The rarefaction parameter δ characterizes the flow and it is given by

$$\delta = \frac{\sqrt{\pi}}{2} \frac{1}{Kn} = \frac{\sqrt{\pi}}{2} \frac{D_h}{\lambda} = \frac{D_h P}{\mu \upsilon}, \tag{17}$$

where $P = P(z)$ is the pressure along the microchannel, μ is the gas viscosity at temperature T and $\upsilon = \sqrt{2RT}$ is the most probable molecular velocity. It is seen that δ is proportional to the inverse Knudsen number, i.e. $\delta = 0$ and $\delta \to \infty$ correspond to the free molecular and hydrodynamic limits, respectively. The gas–wall interaction is modeled by the Maxwell diffuse–specular reflection condition. At the boundaries we have (Naris and Valougeorgis 2008)

$$\Phi^+ = (1 - \alpha)\Phi^- \tag{18}$$

where Φ^+ and Φ^- are the distributions representing particles departing and arriving at the wall, respectively, while the tangential momentum accommodation coefficient α denotes the portion of the particles reflecting diffusively from the wall.

The kinetic problem described by Eqs. 15 and 16 and the associated boundary condition 18 is solved numerically in an iterative manner. The numerical scheme has been presented, in detail, in previous works (Sharipov 1999; Naris and Valougeorgis 2008) and, therefore, only the key elements are presented here for completeness purposes. The two components of the molecular velocity vector are written in terms of polar coordinates as $c_x = \zeta \cos\theta$ and $c_y = \zeta \sin\theta$, where $0 \le \zeta \le \infty$ is its magnitude and $0 \le \theta \le 2\pi$ its polar angle. Then, the discretization in the molecular velocity space is performed by choosing a suitable set of discrete velocities $(\zeta_m,\ \theta_n)$, defined by $0 \le \zeta_m < \infty$ and $0 \le \theta_n \le 2\pi$, with $m = 1,2,\ldots,\ M$ and $n = 1,2,\ldots,\ N$. Introducing this discretization into Eqs. 15 and 16, yields a system of partial differential equations

$$\zeta_m \cos\theta_n \frac{\partial \Phi_{m,n}^{(k+1/2)}}{\partial x} + \zeta_m \sin\theta_n \frac{\partial \Phi_{m,n}^{(k+1/2)}}{\partial y} + \delta \Phi_{m,n}^{(k+1/2)} = \delta u^{(k)} - \frac{1}{2} \tag{19}$$

coupled with the double summations

$$u^{(k+1)} = \sum_n \sum_m w_m w_n \Phi_{m,n}^{(k+1/2)}, \tag{20}$$

where w_m and w_n are the weighting factors corresponding to the integration over ζ_m and θ_n, respectively.

Equations 19 and 20 are solved in an iterative manner, with the superscript k denoting the iteration index. First, the macroscopic velocity $u^{(k)}$ is assumed at the right-hand side of Eq. 19, which is solved for the distribution function $\Phi_{m,n}^{(k+1/2)}$. Then, the distribution function is introduced into Eq. 20 to compute the updated values of the macroscopic velocity $u^{(k+1)}$. This iteration map is terminated when the convergence criterion is fulfilled. In several occasions, it is necessary to speed up the convergence of the iteration scheme by introducing a synthetic diffusion acceleration scheme introduced in (Valougeorgis and Naris 2003). In each iteration, the system of partial differential equations 19 is solved by implementing a second-order central finite difference scheme in the physical space. It is important to note that the system is solved in an explicit manner using a marching procedure and no matrix inversion is required. The implemented numerical algorithm, supplemented by a reasonable dense grid and an adequate large set of discrete velocities, deduces grid-independent results up to several significant figures with modest computational effort.

Once the above-described dimensionless kinetic problem is solved, several dimensional quantities of practical interest may be recovered in a straightforward manner. For the purposes of the present work, we focus on the mass flow rate, which is calculated from (Sharipov and Seleznev 1998; Varoutis et al. 2009) by

$$\dot{M} = G \frac{\tilde{A} D_h}{\upsilon} \frac{\mathrm{d}P}{\mathrm{d}z}. \tag{21}$$

Here, D_h and $\tilde{A}$ are the hydraulic diameter and the cross section area of the microchannel. The quantity G is traditionally known as reduced (or dimensionless) flow rate and it is defined by (Sharipov and Seleznev 1998)

$$G = \frac{2}{A} \iint_A u \, \mathrm{d}A \tag{22}$$

with $A = \tilde{A}/D_h^2$ denoting the dimensionless cross-section area. The kinetic solution, which finally results in the calculation of G, depends only on δ, A, and α.

In the present work, the measured mass flow rates are compared with the computed ones. For this purpose, two approaches are compared. Both of them deduce practically identical results. In the first approach, the mass flow rate is calculated by

$$\dot{M} = G^* \frac{\tilde{A} D_h}{\upsilon} \frac{P_\mathrm{A} - P_\mathrm{B}}{L}. \tag{23}$$

The quantity G^* is computed from the kinetic solver using the specific dimensionless cross section A and an average rarefaction parameter $\delta_0 = (\delta_A + \delta_B)/2$, where δ_A and δ_B correspond to pressures P_A and P_B, respectively, while the accommodation coefficient, α, may vary depending on the roughness of the channel wall. In the same way, the average Knudsen number is defined as $Kn_0 = \sqrt{\pi}/2\delta_0$.

In an alternative approach, the variation of the pressure gradient along the microchannel is taken into account. For that purpose, the value of the reduced flow rate $G(\delta)$ is calculated as a function of δ which varies along the microchannel. The function $G(\delta)$ is fitted with a polynomial approximation as

$$G(\delta) = b_0 + b_1\delta + b_2\delta^2 + b_3\delta^3 + b_4\delta^4 + b_5\delta^5 + b_6\delta^6. \tag{24}$$

Then, Eq. 21 could be written as

$$\dot{M} = \frac{D_h(HB)}{\upsilon}\frac{\mathrm{d}P}{\mathrm{d}z}\left(b_0 + b_1\delta + b_2\delta^2 + b_3\delta^3 + b_4\delta^4 + b_5\delta^5 + b_6\delta^6\right). \tag{25}$$

For an isothermal flow, the ratio of P/δ is constant along the microchannel:

$$\frac{P}{\delta} = \frac{P_B}{\delta_B}. \tag{26}$$

Then Eq. 25 becomes

$$\dot{M} = \frac{D_h(HB)}{\upsilon}\frac{\mathrm{d}P}{\mathrm{d}z} \times \left(b_0 + b_1\delta_B\frac{P}{P_B} + b_2\delta_B^2\left(\frac{P}{P_B}\right)^2 + b_3\delta_B^3\left(\frac{P}{P_B}\right)^3 + b_4\delta_B^4\left(\frac{P}{P_B}\right)^4 + b_5\delta_B^5\left(\frac{P}{P_B}\right)^5 + b_6\delta_B^6\left(\frac{P}{P_B}\right)^6\right). \tag{27}$$

After integration along the microchannel,

$$\dot{M} = \frac{D_h(HB)}{\upsilon}\frac{P_B}{L}\left(b_0(\Pi - 1) + b_1\frac{\delta_B}{2}(\Pi^2 - 1) + b_2\frac{\delta_B^2}{3}(\Pi^3 - 1) + b_3\frac{\delta_B^3}{4}(\Pi^4 - 1) + b_4\frac{\delta_B^4}{5}(\Pi^5 - 1) + b_5\frac{\delta_B^5}{6}(\Pi^6 - 1) + b_6\frac{\delta_B^6}{7}(\Pi^7 - 1)\right). \tag{28}$$

Due to the shape of $G(\delta)$, the polynomial approximation has been done separately for two ranges of the rarefaction number. Corresponding values of coefficients b_i are given in Table 4. Simulated data obtained from Eqs. 23 and 28 have been compared. In most cases, the deviation between the two models has been found negligible: the difference between the two theoretical $\dot{M}(\Pi)$ curves was less than the width of the line. All the following figures represent kinetic results obtained from Eq. 28.

The kinetic analysis and solution methodology described above have been extended to the case of binary gas mixtures through rectangular channels based on the McCormack model (Naris et al. 2005). It is interesting to note that for gas mixtures, the imposed pressure gradient produces two types of flow. The first one, denoted by G_{PP}, is the well-known Poiseuille flow; it is a direct effect and it is the one, which has been extensively studied in the case of single gases. The second one, denoted by G_{CP}, is known as barodiffusion and it is a cross effect, which disappears as the flow is approaching the hydrodynamic limit. Following (Naris et al. 2005) both dimensionless flow rates may be computed. Then, dimensionalizing the results it is deduced that the combined mass flow rate is given by

$$\dot{M} = [G^*_{PP} + G^*_{BD}]\frac{P_A - P_B}{L}\frac{H(HW)}{\upsilon} = G^*_{Cal}\frac{P_A - P_B}{L}\frac{H(HW)}{\upsilon}, \tag{29}$$

where

$$G^*_{BD} = -\frac{(m_2 - m_1)}{m}(1 - C_0)G^*_{CP} \tag{30}$$

C_0 is the molar concentration of the mixture, m_1 and m_2 are the molecular masses of the two species and

$$m = m_1C_0 + (1 - C_0)m_2 \tag{31}$$

is the molecular mass of the mixture. As in the case of simple gases, in order to avoid an estimation of G^*_{PP} and G^*_{CP} based on a mean value of $\delta' = \delta\frac{H}{D_h}$, the mass flow rate can also be obtained by integration of

$$\dot{M} = G_{Cal}(\delta')\frac{\mathrm{d}P}{\mathrm{d}z}\frac{H(HW)}{\upsilon}, \tag{32}$$

which leads to

$$\dot{M} = \frac{H(HB)}{\upsilon}\frac{P_B}{L} \times \left(c_0(\Pi - 1) + c_1\frac{\delta'_B}{2}(\Pi^2 - 1) + c_2\frac{\delta'^2_B}{3}(\Pi^3 - 1)\right), \tag{33}$$

after a polynomial fit of $G_{Cal}(\delta') = G_{PP}(\delta') + G_{BD}(\delta')$. Values of coefficients c_i are given in Table 5, and Sect. 4.3 provides a comparison between data obtained from Eqs. 29 and 33.

Closing this section, it is noted that the implementation of the linearized BGK and McCormack models for solving rarefied flows through microchannels is valid, not only in small but even at arbitrarily large pressure drops, provided that the ratio of the hydraulic diameter over the length of the channel is much less than one. This is the same assumption which allows the modeling of the flow as a

Table 4 Coefficients for $G(\delta)$ as a function of α for $a^* = 0.089$

δ	α	b_0	b_1	b_2	b_3	b_4	b_5	b_6
0.2–7	0.9	1.097E + 00	−3.715E − 01	2.521E − 01	−8.502E − 02	1.557E − 02	−1.445E − 03	5.312E − 05
	1	9.516E − 01	−3.037E − 01	2.070E − 01	−6.927E − 02	1.264E − 02	−1.170E − 03	4.295E − 05
7–65	0.9	7.207E − 01	4.387E − 02	2.717E − 05	–	–	–	–
	1	6.209E − 01	4.357E − 02	2.994E − 05	–	–	–	–

Table 5 Coefficients for $G_{\mathrm{Cal}}(\delta')$ as a function of α for $a^* = 0.089$

δ'	α	c_0	c_1	c_2
9–30	0.9	1.371E + 00	1.523E − 01	8.038E − 05
	1	1.172E + 00	1.514E − 01	9.410E − 05

linear fully developed flow (Sharipov 1999; Varoutis et al. 2009).

4 Results and discussion

Experiments have been carried out for moderate Knudsen numbers in the slip flow regime and higher Knudsen numbers in the transition regime, based on two different values of the downstream pressure. The upstream pressure has been changed to obtain different upstream over downstream pressure ratios. The data are presented either as mass flow rate versus pressure ratio or as reduced flow rate versus rarefaction parameter.

4.1 Experimental comparisons between CV and DT methods for moderate Knudsen numbers

The CV method can be implemented for all the range of Knudsen numbers investigated in the present paper. On the other hand, the DT method is limited to relatively high-operating pressures for two reasons. First, for low-operating pressures, outgassing is no longer negligible and would affect the liquid drop velocity. Taking this effect into account would require a monitoring of the pressure variation, leading to a hybrid method combining DT and CV methods. Second, if the drop is a drop of water, its movement is smooth and allows accurate velocity tracking. However, for low pressures, vaporization of the water could occur. This issue could be resolved using a drop of glycerin or oil with low-saturated vapor pressure; however, these liquids are much more wetting than water, and would require a better hydrophobic treatment of the inside surface of the pipette. Consequently, for these reasons, all the experimental data presented in this paper have been done with the CV method.

However, we have compared the two methods in the range $10 < \delta_0 < 45$. Figure 7 shows a good agreement between the experimental data obtained with the CV method and previous detailed data obtained with the DT method with a simpler setup in the same team (Lalonde 2001; Colin et al. 2004). A few experiments have been done with the novel setup with the DT method, and the obtained data were consistent with the previous data presented in Fig. 7. It is one of our future objectives to extend the use of the DT method to higher Knudsen numbers (i.e. to lower rarefaction parameters), using for example microchannels with lower hydraulic diameters which would allow higher rarefaction with the same level of pressure.

4.2 Experimental data for single monatomic gases

Experimental work has been carried out with Ar and He for two different values of the downstream pressure P_B equal about to 5×10^4 and 2×10^3 Pa. The upstream pressure P_A is controlled in order to obtain different values of the pressure ratio $\Pi = P_A/P_B$ between 1.4 and 6.6.

The experimental data and results, for both gases, are tabulated in Table 2, where for each experimental run in addition to the pressure ratio, the measured upstream and downstream pressures as well as the estimated mass flow rates at the inlet and the outlet of the microsystem, $\dot{M}_A$ and $\dot{M}_B$, respectively, are presented. It is noted that the tabulated values of P_B vary slightly at each experimental run from the ones mentioned earlier. Based on the measured pressures, the gas characteristics and the geometry of the channel, it is easily found that $0.02 \leq Kn \leq 1.5$ (or $44 \geq \delta \geq 0.6$). Therefore, the slip regime as well as significant part of the transition regime are covered. These two regimes are indicated in Table 6 as moderate and high Knudsen number areas, corresponding to pressure ratios smaller and larger than $\Pi = 3$, respectively. It is noted that in all cases $\dot{M}_A \simeq \dot{M}_B$.

Comparing the mass flow rates of Ar and He, it is seen that for approximately the same upstream and downstream pressures, the mass flow rate of Ar is always larger than the corresponding one of He. It is also noted that the Knudsen number characterizing the flow in the cases of Ar and He is not the same, even when the upstream and downstream pressures are the same. This is due to different viscosities

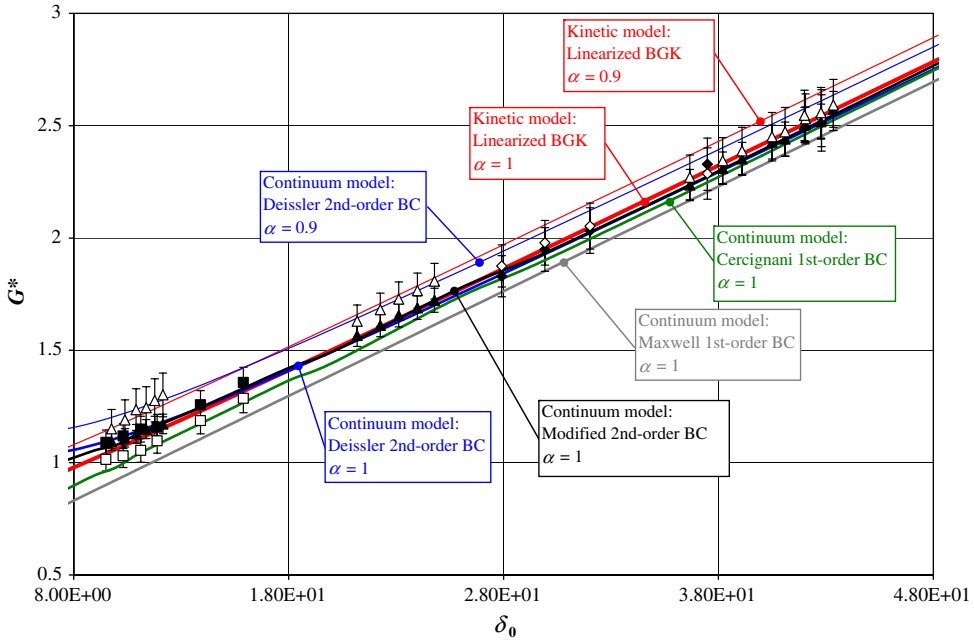

Fig. 7 Reduced flow rate versus rarefaction factor. Experimental data obtained with the CV method: inlet (*filled square*) and outlet (*open square*) data for helium and inlet (*filled diamond*) and outlet (*open diamond*) data for argon, detailed in Figs. 11 and 12. Experimental data obtained with the DT method: inlet (*filled triangle*) and outlet (*open triangle*) data for helium, from (Lalonde 2001). Comparison with kinetic and continuum models

Table 6 Experimental data, for Argon and Helium at constant temperature $T = 298.5$ K

	Kn_0	Π	P_A	P_B	$\dot{M}_A$	$\dot{M}_B$	Uncertainty (%)	
			Pa		kg/s		*A*	*B*
Argon								
Moderate Knudsen number	2.1E − 02	2.99	149,687	50,074	1.95E − 11	1.97E − 11	4.0	4.0
	2.4E − 02	2.50	125,056	49,927	1.37E − 11	1.34E − 11	4.0	4.0
	2.8E − 02	1.98	99,288	50,169	7.80E − 12	7.88E − 12	4.0	4.0
	3.0E − 02	1.79	89,862	49,828	6.09E − 12	6.19E − 12	4.0	4.0
	3.2E − 02	1.60	80,124	50,158	4.28E − 12	4.39E − 12	4.0	4.0
	3.4E − 02	1.38	69,764	50,399	2.5E − 12	2.7E − 12	4.0	4.0
High Knudsen number	2.6E − 01	6.61	13,569	2,052	7.47E − 13	7.18E − 13	6.0	6.6
	3.0E − 01	5.96	11,857	1,990	6.06E − 13	6.05E − 13	6.8	7.5
	3.5E − 01	4.79	9,754	2,036	4.84E − 13	4.77E − 13	7.3	7.8
	4.2E − 01	4.02	7,879	1,962	3.59E − 13	3.49E − 13	8.6	8.6
	5.0E − 01	3.10	6,198	2,002	2.66E − 13	2.55E − 13	9.7	9.6
Helium								
Moderate Knudsen number	5.7E − 02	2.90	148,460	51,190	3.26E − 12	3.09E − 12	4.0	4.0
	6.5E − 02	2.42	123,610	50,990	2.26E − 12	2.13E − 12	4.0	4.0
	7.6E − 02	1.95	98,760	50,540	1.38E − 12	1.31E − 12	4.0	4.0
	8.1E − 02	1.72	88,440	51,300	1.06E − 12	9.68E − 13	4.0	4.0
	8.8E − 02	1.58	79,150	50,210	8.00E − 13	7.37E − 13	4.0	4.0
	9.5E − 02	1.44	70,373	48,890	5.79E − 13	5.39E − 13	4.0	4.0
High Knudsen number	7.3E − 01	6.81	13,489	1,982	2.16E − 13	2.20E − 13	4.5	4.9
	8.4E − 01	5.83	11,576	1,985	1.87E − 13	1.84E − 13	4.8	5.0
	9.4E − 01	4.97	10,015	2,015	1.53E − 13	1.52E − 13	5.1	5.3
	1.1E + 00	3.92	7,870	2,008	1.14E − 13	1.09E − 13	5.6	6.0
	1.4E + 00	3.12	6,020	1,928	7.78E − 14	7.82E − 14	6.6	6.4

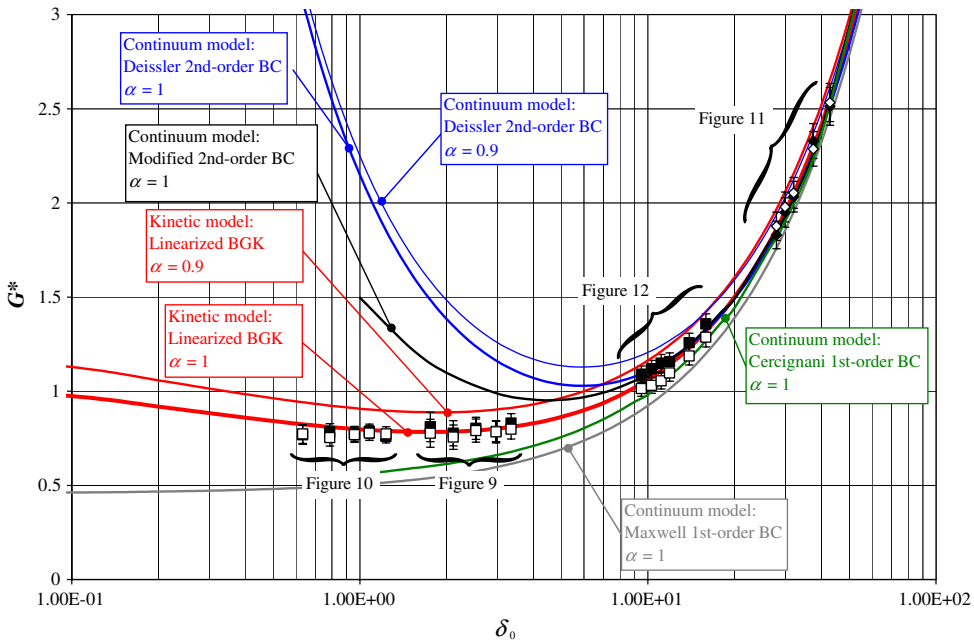

Fig. 8 Reduced flow rate versus rarefaction factor. Comparison between inlet (*filled square*) and outlet (*open square*) data for helium and inlet (*filled diamond*) and outlet (*open diamond*) data for argon with kinetic and continuum models. Data from Table 6. $T = 298.5$ K

and molecular velocities. Actually, for the same pressure set up, the Knudsen number for the light gas is larger.

We continue with a detailed comparative study between experiments and calculations presented in Figs. 8, 9, 10, 11, 12. First, an overall view of the experimental and the associated computed results is shown in Fig. 8, where the reduced flow rate G is plotted in terms of the rarefaction parameter δ_0. Experimental data obtained with Ar and He are represented with diamond-shaped and square symbols, respectively. Experimental uncertainties on G, deduced from the uncertainties of the mass flow rate $\dot{M}$ (see Eq. 7), are represented by vertical bars. Also, continuum and kinetic model computed results are provided for $\alpha = 1$ and 0.9.

It is observed that the experimental data are in very good agreement with the kinetic model based on the linearized BGK equation, with $\alpha = 1$, in the whole range of δ for both Ar and He. It is interesting to note that based on the experimental work, we may deduce that for both gases the interaction with the wall is purely diffusive. Regarding the continuum models, it is seen that all models perform quite well for $\delta_0 \geq 20$, while as δ_0 is further decreased they gradually deviate from the measured flow rate. In particular, the first-order model underestimates, while the second-order models overestimate the values of G. It may be argued, as it is seen from the modified boundary conditions, that for this specific problem, second-order models remain reliable even for values of δ_0 a little bit less than 10.

Ewart et al. studied the flow of monatomic gases through rectangular microchannels with a low-aspect ratio $a^* = 2\%$ (Ewart 2007; Ewart et al. 2007). With such an aspect ratio, the flow is close to a 2-D flow between parallel plates. The authors found a good agreement between their experimental data and a kinetic BGK model, down to an average rarefaction parameter $\delta_0 \approx 0.2$. A quantitative comparison of their data with the present data is not possible, as the rectangular microchannel considered here has a high-aspect ratio $a^* = 9\%$ which leads to non-negligible 3-D effects. However, Fig. 8 extends the main conclusions from Ewart et al., showing that a kinetic BGK model is accurate for gas flows in rectangular microchannels.

The results of Table 6 and Fig. 8 are examined more thoroughly in Figs. 9, 10, 11, 12, where the mass flow rates $\dot{M}$ are plotted in terms of the pressure ratio Π. In particular, the results for the high Knudsen number ($\delta_0 < 5$), corresponding to a pressure ratio from 3 to 7, are plotted in Fig. 9 for Ar and in Fig. 10 for He. Similarly, the results for the moderate Knudsen number ($\delta_0 > 5$), corresponding to a pressure ratio from 1.4 to 3, are plotted in Fig. 11 for Ar and in Fig. 12 for He. The range of the average Knudsen number is indicated in the legend of each figure. As the downstream pressure P_B can slightly differ at each experimental run (within $\pm 2\%$ around the values 2×10^3 Pa, in Figs. 9 and 10, or around 5×10^4 Pa, in Figs. 11 and 12), and as the mass flow rate depends both on the pressure ratio and on the downstream pressure, all theoretical data have been calculated for the exact values of P_B provided in Table 6. This is the reason why some theoretical curves can experience small irregularities.

The very good agreement between experimental and kinetic results, with $\alpha = 1$, is clearly demonstrated through all Figs. 9, 10, 11, 12. Also, the effect of the tangential momentum accommodation coefficient on the mass flow rates may be observed by comparing the kinetic results for $\alpha = 1$ with the corresponding ones for $\alpha = 0.9$. As

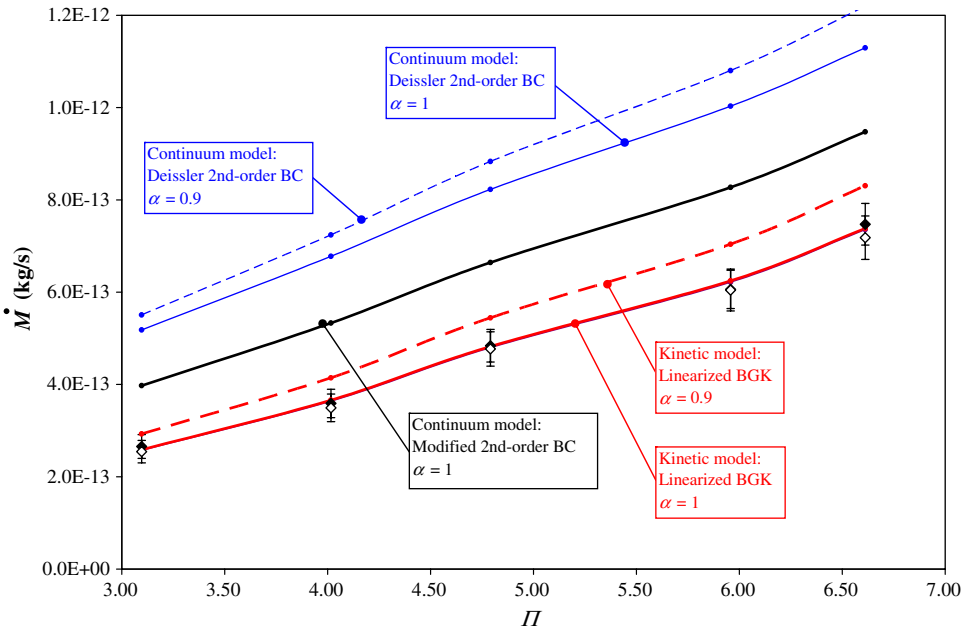

Fig. 9 Mass flow rate versus pressure ratio for argon. Comparison between inlet (*filled diamond*) and outlet (*open diamond*) data with kinetic and continuum models. Data from Table 6. $T = 298.5$ K, $P_B \approx 2 \times 10^3$ Pa, $0.25 < Kn_0 < 0.5$, $1.7 < \delta_0 < 3.4$

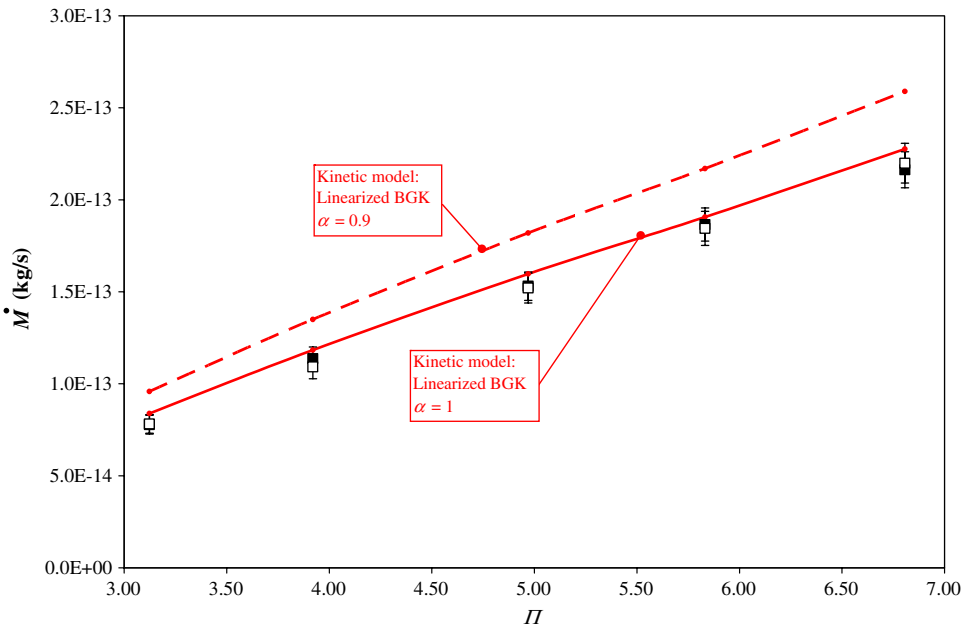

Fig. 10 Mass flow rate versus pressure ratio for helium. Comparison between inlet (*filled square*) and outlet (*open square*) data with kinetic models. Data from Table 6. $T = 298.5$ K, $P_B \approx 2 \times 10^3$ Pa, $0.7 < Kn_0 < 1.5$, $0.6 < \delta_0 < 1.2$

expected, as the rarefaction is increased, the dependency of $\dot{M}$ on α is also increased.

In Fig. 9, the limits of the continuum model with second-order boundary conditions from Deissler are clearly pointed out. It is seen that the discrepancy between second-order slip theory and measurements (or kinetic theory) is significant. The modified second-order boundary conditions provide improved results, which are closer to the kinetic results, but again the correct values of the flow rates are overestimated.

Similar observations can be made in the case of He, in Fig. 10. Here, as mentioned earlier, the corresponding Knudsen numbers are higher compared to the ones in the experiment with Ar, and, therefore, the discrepancy between the continuum model and measured (or kinetic theory) flow rates becomes more significant. For this reason, we have decided not to show the continuum results in this figure since they are out of the scale used in the figure.

On the other hand, for moderate Knudsen numbers as the ones in Figs. 11 and 12 continuum models perform much better. In particular, the modified second-order slip model is in very good agreement with the experimental results, assuming $\alpha = 1$, as it is also found with the BGK kinetic model. Although the accommodation coefficient can be determined with a precision of a few percents only,

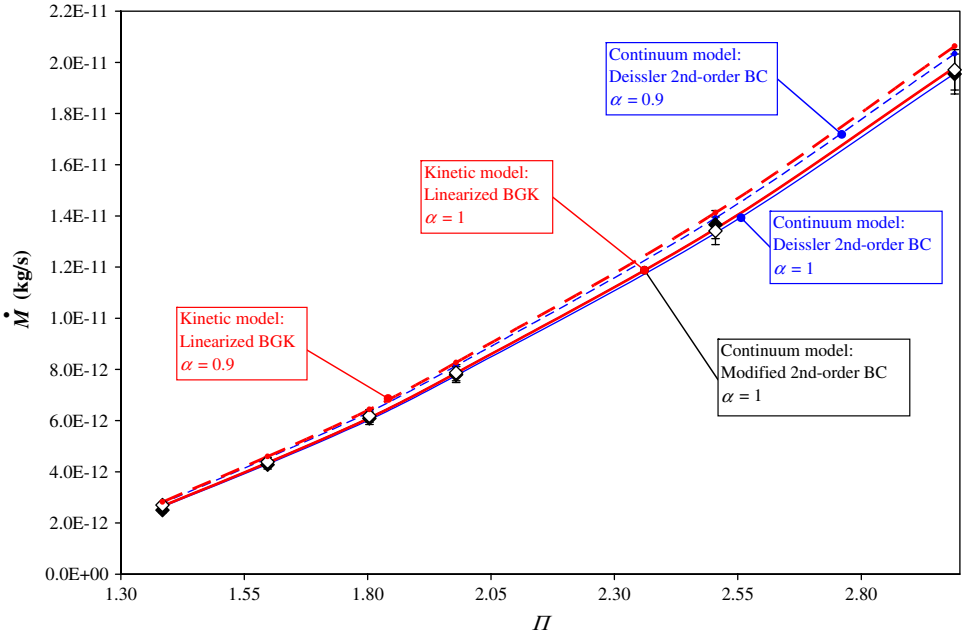

Fig. 11 Mass flow rate versus pressure ratio for argon. Comparison between inlet (*filled diamond*) and outlet (*open diamond*) data with kinetic and continuum models. Data from Table 6. $T = 298.5$ K, $P_B \approx 5 \times 10^4$ Pa, $0.021 < Kn_0 < 0.034$, $25.7 < \delta_0 < 42.8$

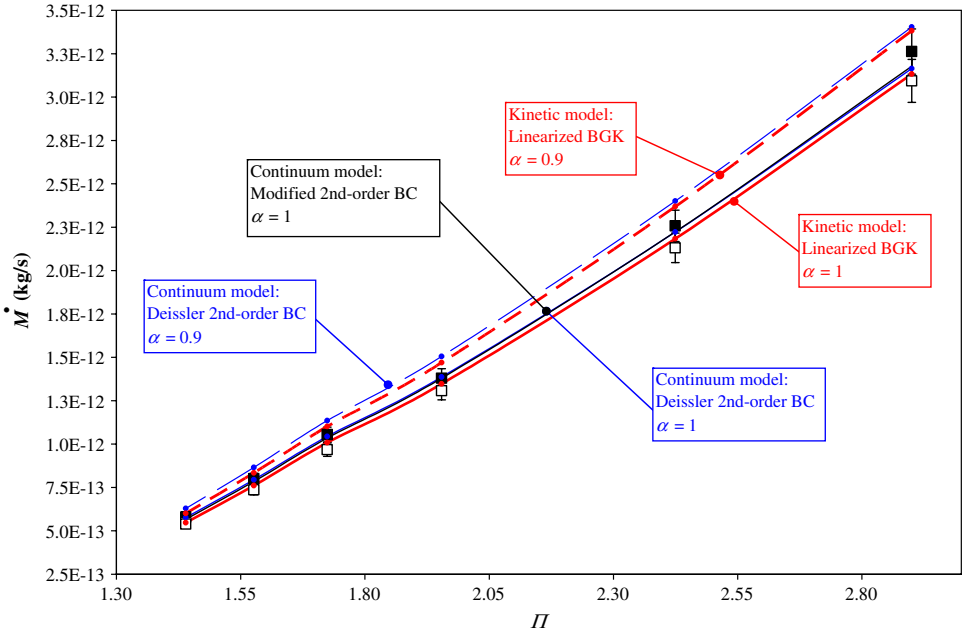

Fig. 12 Mass flow rate versus pressure ratio for helium. Comparison between inlet (*filled square*) and outlet (*open square*) data with kinetic and continuum models. Data from Table 6. $T = 298.5$ K, $P_B \approx 5 \times 10^4$ Pa, $0.057 < Kn_0 < 0.095$, $9.3 < \delta_0 < 15.6$

due to experimental uncertainties, it could be concluded that in average, the accommodation of the gas molecules on the microchannel walls is essentially diffuse.

4.3 Data on binary mixture

A first set of experimental data for a binary mixture of monatomic gases is now presented in Fig. 13. The mixture is composed of 30% He and 70% Ar. In these experiments, the Knudsen number is less than 0.04 and therefore, the flow is in the slip regime. Tabulated results are presented in Table 7, where experimental and kinetic results may be compared. The agreement is very good. In addition, the portion of the flow which is due to the classical Poiseuille flow and due to barodiffusion indicated by G^*_{PP} and G^*_{BD}, respectively, are specified in the last two columns of the table. It is seen that in the slip regime, the contribution of barodiffusion is negligible.

Experimental data are compared to the second-order continuum models, considering the binary mixture as a single gas with properties deduced from the properties of each gas taking into account the proportion of each species in the mixture. As seen in Fig. 13, the agreement between experiments and computations from the continuum model associated with

Table 7 Experimental and computational data, for a binary mixture of Ar–He at constant temperature $T = 298.5$ K

He (30%)–Ar (70%)										
Kn_0	Measurement					Calculation $\alpha = 1$				
	Π	P_A	P_B	$\dot{M}_A$	$\dot{M}_B$	$\dot{M}$ – Eq. (33)	$\dot{M}$ – Eq. (29)	G^*_{Cal}	G^*_{PP}	G^*_{BD}
2.5E − 02	2.99	150,093	50,151	1.53E − 11	1.50E − 11	1.519E − 11	1.518E − 11	4.184	4.222	−0.037
2.8E − 02	2.50	125,256	50,112	1.05E − 11	1.03E − 11	1.038E − 11	1.038E − 11	3.805	3.848	−0.042
3.3E − 02	2.01	100,190	49,914	6.32E − 12	6.24E − 12	6.247E − 12	6.244E − 12	3.422	3.471	−0.049
3.5E − 02	1.80	89,779	49,943	4.74E − 12	4.73E − 12	4.723E − 12	4.720E − 12	3.265	3.317	−0.052
3.8E − 02	1.63	80,567	49,577	3.39E − 12	3.51E − 12	3.511E − 12	3.509E − 12	3.120	3.176	−0.056

All uncertainties are ±4.0%

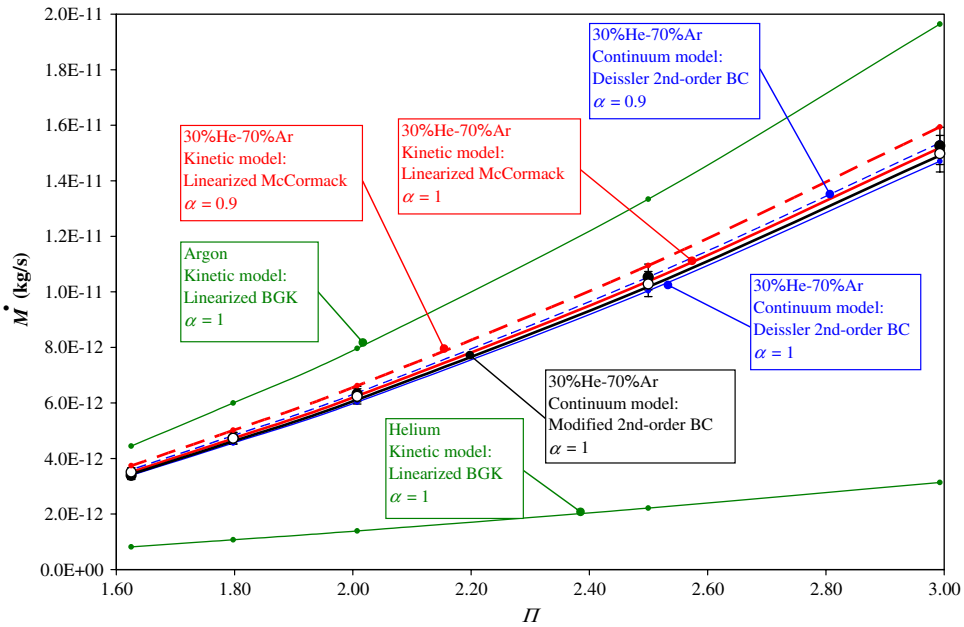

Fig. 13 Mass flow rate versus pressure ratio for a mixture of He (30%) and Ar (70%). Comparison between inlet (*filled circle*) and outlet (*open circle*) data with kinetic and continuum models. Data from Table 7. $T = 298.5$ K, $P_B \approx 5 \times 10^4$ Pa, $0.025 < Kn_0 < 0.038$, $23.5 < \delta_0 < 36.1$

second-order modified boundary conditions is very good and coherent with data relative to single gases (see Figs. 11 and 12). In Fig. 13, the computational curves for Ar and He single gases have been added for comparison purposes.

Finally, it should also be pointed out that this comparison between experiments and theory for a mixture is preliminary and that more detailed and complete results will be presented in the near future. For higher rarefied flows, the hypothesis that the concentration of the species is the same in the reservoirs and in the microchannels could be no longer valid, and the model proposed in Sect. 3.2 as well as the experimental data processing should be modified.

5 Conclusions and perspectives

The description and validation of a new experimental setup for accurate gas micro flow rate measurement has been presented. The main advantages of this setup are

- The possibility to use two complementary measurement methods (a direct one, the "DT method" and an indirect one, the "CV method");
- the double measurement upstream and downstream from the microsystem; and
- its thermal regulation.

Experimental data for monatomic gases flowing through rectangular microchannels have been obtained in the slip flow and transition regimes and compared with continuum and kinetic models. A very good agreement has been found by assuming diffuse reflection of the molecules with complete accommodation at the walls, and by taking into account the 3-D geometry of the microchannel. Finally, a first set of experimental data have been obtained for mixtures of gases.

Additional investigation is currently under process, especially for other mixtures of gases with various concentrations in a wider range of the Knudsen number. Modifications of the model, as well as of the experimental

data processing, will be made for mixtures of gases in the transition regime.

Acknowledgments The support of the European Community under grant PITN-GA-2008-215504, 'Gas flows in Micro Electro Mechanical Systems', and the support of EGIDE under grant PHC-15080QE, 'Ecoulements types de mélanges gazeux dans les nano et microsystèmes à vocation biologique" are gratefully acknowledged.

References

Arkilic EB, Breuer KS et al (2001) Mass flow and tangential momentum accommodation in silicon micromachined channels. J Fluid Mech 437:29–43

Aubert C, Colin S (2001) High-order boundary conditions for gaseous flows in rectangular microchannels. Microscale Thermophys Eng 5(1):41–54

Bergoglio M, Calcatelli A et al (1995) Gas flow rate measurements for leak calibration. Vacuum 46(8–10):763–765

Cercignani C, Daneri A (1963) Flow of a rarefied gas between two parallel plates. J Appl Phys 34(12):3509–3513

Cercignani C, Illner R et al (1994) The mathematical theory of dilute gases. Springer, New York

Chapman S, Cowling TG (1952) The mathematical theory of non-uniform gases. University Press, Cambridge

Colin S (2005) Rarefaction and compressibility effects on steady and transient gas flows in microchannels. Microfluid Nanofluid 1(3):268–279

Colin S, Lalonde P et al (2004) Validation of a second-order slip flow model in rectangular microchannels. Heat Transf Eng 25(3):23–30

Deissler RG (1964) An analysis of second-order slip flow and temperature-jump boundary conditions for rarefied gases. Int J Heat Mass Transf 7:681–694

Ewart T (2007) Etude des écoulements gazeux isothermes en microconduit: du régime hydrodynamique au proche régime moléculaire libre. PhD Thesis Report, Ecole Polytechnique Universitaire de Marseille, France

Ewart T, Perrier P et al (2006) Mass flow rate measurements in gas micro flows. Exp Fluids 41(3):487–498

Ewart T, Perrier P et al (2007) Mass flow rate measurements in a microchannel, from hydrodynamic to near free molecular regimes. J Fluid Mech 584:337–356

Hadjiconstantinou NG (2003) Comment on Cercignani's second-order slip coefficient. Phys Fluids 15(8):2352–2354

Harley JC, Huang Y et al (1995) Gas flow in micro-channels. J Fluid Mech 284:257–274

Jousten K, Menzer H et al (2002) A new fully automated gas flowmeter at the PTB for flow rates between 10–13 mol/s and 10–6 mol/s. Metrologia 39(6):519–529

Kandlikar SG, Garimella S et al (2006) Heat transfer and fluid flow in minichannels and microchannels. Elsevier, Oxford

Lalonde P (2001) Etude expérimentale d'écoulements gazeux dans les microsystèmes à fluides. PhD Thesis Report, Institut National des Sciences Appliquées de Toulouse, France

Maurer J, Tabeling P et al (2003) Second-order slip laws in microchannels for helium and nitrogen. Phys Fluids 15(9):2613–2621

Maxwell JC (1879) On stresses in rarefied gases arising from inequalities of temperature. Philos Trans R Soc Lond 170:231–256

McCulloh KE, Tilford CR et al (1987) Low-range flowmeters for use with vacuum and leak standards. J Vac Sci Technol A 5(3):376–381

Naris S, Valougeorgis D (2008) Rarefied gas flow in a triangular duct based on a boundary fitted lattice. Eur J Mech B Fluids 27(6):810–822

Naris S, Valougeorgis D et al (2005) Flow of gaseous mixtures through rectangular microchannels driven by pressure, temperature, and concentration gradients. Phys Fluids 17(10): 100607:1–12

Pong K-C, Ho C-M et al (1994) Non-linear pressure distribution in uniform microchannels. In: Bandyopadhyay PR, Breuer KS, Blechinger CJ (Eds). Application of microfabrication to fluid mechanics. ASME, New York, FED-197: 51–56

Sharipov F (1999) Rarefied gas flow through a long rectangular channel. J Vac Sci Technol A 17(5):3062–3066

Sharipov F, Seleznev V (1998) Data on internal rarefied gas flows. J Phys Chem Ref Data 27(3):657–706

Valougeorgis D, Naris S (2003) Acceleration schemes of the discrete velocity method: gaseous flows in rectangular microchannels. SIAM J Sci Comput 25(2):534–552

Varoutis S, Naris S et al (2009) "Computational and experimental study of gas flows through long channels of various cross sections in the whole range of the Knudsen number. J Vac Sci Technol A 27(1):89–100

Zohar Y, Lee SYK et al (2002) Subsonic gas flow in a straight and uniform microchannel. J Fluid Mech 472:125–151